Detection of Apoptotic Cell Death In Vitro in the Presence of Gd-DTPA-BMA

Colleen Bailey,[1,2*] Anoja Giles,[3] Gregory J. Czarnota,[1–3] and Greg J. Stanisz[1,2]

Due to variability in patient response to cancer therapy, there is a growing interest in monitoring patient progress during treatment. Apoptotic cell death is one early marker of tumor response to treatment. Using known extracellular concentrations of gadolinium diethylenetriamine pentaacetic acid bismethylamide (Gd-DTPA-BMA) to vary the exchange regime, T_1 and T_2 relaxation data for acute myeloid leukemia (AML) cell samples were obtained and then analyzed using a two-pool model of relaxation with exchange. Leukemia cells treated with cisplatin to induce apoptosis exhibited a statistically significant ($P < 0.05$) decrease in intracellular longitudinal relaxation time, T_{1I}, from 1030 ms to 940 ms, a decrease ($P < 0.001$) in the intracellular water fraction, M_{0I}, from 0.86 to 0.68 and a statistically significant increase ($P < 0.01$) in transmembrane water exchange rate, k_{IE}, from 1.4 s^{-1} to 6.8 s^{-1}. The changes in MR parameters correlated with quantitative histology, such as cellular cross-sectional area and average nuclear area measurements. The results of this study emphasize the importance of accounting for water exchange in dynamic contrast-enhanced MRI (DCE-MRI) studies, particularly those that examine tumor response to therapies in which apoptotic changes occur. Magn Reson Med 62:46–55, 2009. © 2009 Wiley-Liss, Inc.

Key words: apoptosis; water exchange; T_1 relaxation; T_2 relaxation; tumor response

Due to the large number of genetic mutations involved in cancer, and the subsequent genetic instability, there is a wide range of response to therapy. There is therefore a growing interest in developing individually-tailored therapies in which treatment is modified according to patient response. For example, many patients with locally-advanced or locoregional disease now receive chemotherapy before surgery and tumor response is assessed using noninvasive imaging. The majority of imaging methods have used posttreatment tumor volume (1) or vascular changes (2,3) occurring as a result of therapeutic treatment as an indicator of response.

Many radiotherapy and chemotherapy regimens can result in cell death by apoptosis. Apoptosis precedes tumor shrinkage and has been correlated with tumor regression (4,5). It has been suggested (6,7) that imaging methods that detect signs of apoptosis can determine the likelihood of response much earlier than tumor volume measurements.

In apoptotic cell death, the cell contents are broken down and distributed in a controlled way for destruction by macrophages or reuse by neighboring cells (8). Characteristic changes include DNA breakdown, condensation and fragmentation of the nuclear material, alterations in cell membrane shape for vesicle formation (membrane blebbing), and an overall decrease in cell size. Significant alteration in cellular architecture is readily apparent with apoptosis.

MRI has been postulated as a structure-sensitive, noninvasive modality, demonstrating sensitivity to small modifications in tissue structure, such as cellular swelling in stroke (9), inflammation (10), and necrosis (11). It is therefore surprising that, despite several attempts to use conventional MRI to probe apoptosis, sensitivity to this process is relatively modest (12–14). The goal of this study was to understand the mechanisms of MR contrast in a model system undergoing apoptosis in order to improve MRI sensitivity and specificity in assessing tumor microstructure following therapy.

There have been a number of attempts to evaluate apoptosis by various imaging methods. Single-photon emission computed tomography (SPECT), optical (15), or MRI (16,17) agents for molecular imaging have been successfully targeted to the lipid phosphatidylserine, which translocates from the inner to the outer leaflet of the plasma membrane early in apoptosis. Moreover, it has been shown that high-frequency ultrasound (18) measurements of back-scattered intensity can distinguish between normal and apoptotic cells in cell samples, tissue, and tumors. In particular, magnetic resonance spectroscopy (MRS) has demonstrated increased lipid mobility (19,20), which indicates the presence of lipid droplets, and increased choline levels (7), which indicates changes in glycolysis and in the phosphatidylcholine synthesis pathways. MRI diffusion shows promise in detecting the decreased cellularity and increased extracellular water content at late stages of apoptosis (12,13) and can indicate changes in cell membrane permeability (21). Many of these methods are limited in resolution (e.g., SPECT, MRS), depth penetration (e.g., optical, ultrasound), or the availability of targeted contrast agents (molecular imaging). Routine clinical application of diffusion measurements also can be limited by low specificity, complex data analysis, and the gradient strength required for improved sensitivity.

To date, conventional MRI relaxation measurements have shown changes only at very late stages of apoptosis. For example, Valonen et al. (13) have demonstrated an increase in the transverse relaxation time constant, T_2, 4 d after induction of apoptosis. Chenevert et al. (12) have observed an increase in T_2 and a slightly smaller increase

[1]Department of Medical Biophysics, Faculty of Medicine, University of Toronto, Toronto, Ontario, Canada.

[2]Imaging Research, Sunnybrook Health Sciences Centre, Toronto, Ontario, Canada.

[3]Department of Radiation Oncology, Faculty of Medicine, University of Toronto and Sunnybrook Health Sciences Centre, Toronto, Ontario, Canada.

Grant sponsors: National Cancer Institute of Canada; Terry Fox Programme.

*Correspondence to: Colleen Bailey, Sunnybrook Health Sciences Centre, 2075 Bayview Ave., S-Wing, 6th floor, Rm S612, Toronto, ON, Canada M4N 3M5. E-mail: colleen.bailey@sri.utoronto.ca

Received 11 August 2008; revised 5 December 2008; accepted 4 January 2009.

DOI 10.1002/mrm.21972

Published online 27 February 2009 in Wiley InterScience (www.interscience.wiley.com).

in longitudinal relaxation time, T_1, 6–8 d after the induction of apoptosis. Duvvuri et al. (14) have reported an increasing trend in T_2 relaxation time, but noted no statistically significant changes within the 36 h following treatment. The low MRI sensitivity to early stages of apoptosis is surprising given the significant changes in tissue chemical and structural composition, such as breakdown in macromolecules, changes in lipid membrane structure, and cellular shrinkage.

One plausible explanation of such a modest sensitivity of the standard MRI methods is the relative simplicity of the methods used to analyze longitudinal and transverse relaxation. The studies to date have assumed monoexponential T_1 and T_2 relaxation behavior, implying that a single effective relaxation describes all water molecules in a measured voxel. This assumption may be generally valid since the intracellular and extracellular relaxation rates in cells are similar and are considered to be slow relative to the exchange of water across the plasma membrane. This exchange regime is often referred to as the fast exchange limit (FXL). In the FXL, the apparent T_1 and T_2 relaxation times in the measured voxel, T_1 and T_2, are an average of the relaxation rates of the intracellular and the extracellular water weighted by their water fractions:

$$\frac{1}{\langle T_1 \rangle} = \frac{M_{0I}}{T_{1I}} + \frac{M_{0E}}{T_{1E}} \qquad [1.1]$$

$$\frac{1}{\langle T_2 \rangle} = \frac{M_{0I}}{T_{2I}} + \frac{M_{0E}}{T_{2E}}, \qquad [1.2]$$

where M_{0I} is the intracellular water fraction, M_{0E} is the extracellular water fraction, $1/T_{1I}$ and $1/T_{1E}$ are the longitudinal relaxation rates of water in the intracellular and extracellular environments, respectively, and $1/T_{2I}$ and $1/T_{2E}$ are the transverse relaxation rates in the intracellular and extracellular environments, respectively.

Nevertheless, it has been shown (22) that the addition of gadolinium-based (Gd) contrast agents may significantly increase the extracellular relaxation rates, $1/T_{1E}$ and $1/T_{2E}$, and make the FXL assumption, and hence Eqs. [1.1] and [1.2], invalid. Using a sufficient number of appropriate Gd concentrations (i.e., significant range of extracellular relaxation times), it is possible to determine intracellular and extracellular relaxation times, water fractions, and the water exchange rate, revealing the intrinsic characteristics of tissue relaxation with apoptosis.

The purpose of this study was to evaluate intracellular and extracellular relaxation and intercompartmental exchange and to examine how they change in apoptotic cells.

MATERIALS AND METHODS

Sample Preparation

For this study, an acute myeloid leukemia cell line (AML-5) was used since its apoptotic properties are well established (18), it can be easily grown, and it can be centrifuged into a sample that mimics a tissue environment. At the same time, investigation in vitro allows apoptotic effects to be studied without the confounding effect of the vasculature and extracellular matrix.

Approximately 1×10^8 AML-5 cells were grown at 37°C with 5% CO_2 in 32 flasks, each containing 150 ml α minimal media (Invitrogen Canada, Inc., Burlington, ON, Canada), 25 ml fetal bovine serum (Fisher Scientific, Ottawa, ON, Canada), and 5 ml penicillin and streptomycin (Invitrogen Canada, Inc.). Apoptosis was induced in one-half of the flasks using cisplatin (10 μg/ml). Cisplatin is a common cancer chemotherapy drug that intercalates with DNA, impairing DNA replication and repair. The degree of cellular apoptosis was evaluated using light and phase microscopy.

At 36 h after cisplatin treatment, cell suspensions were prepared in phosphate-buffered saline (PBS; Invitrogen Canada, Inc.). In order to form samples for MRI, 700 μl of suspended cells, to which gadolinium diethylenetriamine pentaacetic acid bismethylamide (Gd-DTPA-BMA) (Omniscan; GE Healthcare) was added, were placed in MR-compatible glass sample tubes (6-mm-diameter × 50 mm) and centrifuged at 2900*g*. Each experiment consisted of eight cell samples, four control and four treated, with a different Gd-DTPA-BMA concentration, in the range of 0 mM to ~5 mM. A layer of PBS containing Gd-DTPA-BMA remained above the sample, which could be imaged to determine the extracellular Gd-DTPA-BMA concentration. The experiment was repeated five times to determine reproducibility.

MR Acquisition

All MRI experiments were performed on a 3T scanner (GE Signa; GE Medical Systems, Milwaukee, WI, USA) using the body coil to transmit the radiofrequency pulses and a custom-built surface coil (2.5 cm × 4.5 cm) for the received signal. Two coronal slices of 4-mm thickness were acquired: one image 5 mm from the bottom of the cell sample and one reference image in the middle of the PBS layer above the pellet to assess relaxation times of the media, assumed to be equal to T_{1E} and T_{2E}. All images had a field of view = 8 × 8 cm^2 and matrix size = 128 × 128. To measure T_1 relaxation, a standard inversion-recovery (IR) sequence (23) was used (echo time [TE] = 11 ms, repetition time [TR] = 2500 ms, IR time was varied at TI = 50, 100, 200, 300, 500, 700, 900, 1500 ms). T_2 relaxation data were acquired using a modified Carr Purcell Meiboom Gill (CPMG) sequence (24) with 48 echoes (TE = 11.4 ms, TR = 2500 ms, number of excitations [NEX] = 2, and phase cycling of the 180° composite pulses). Crusher gradients of decreasing amplitude were used around the 180° refocusing pulses.

MR Data Analysis

Regions of interest (ROIs) within each sample tube were manually selected for analysis. A typical ROI consisted of 15 voxels. The resulting signal-to-noise ratio within the tubes was approximately 200 for the first echo of the CPMG images, with some dependence on the tube location relative to the surface coil.

Data from the cell pellet were fit using a two-pool model of T_1 and T_2 relaxation (25), as shown in Fig. 1. The intracellular (I) and extracellular (E) compartments, with relative spin densities M_{0I} and M_{0E} ($M_{0I} + M_{0E} = 1$), were

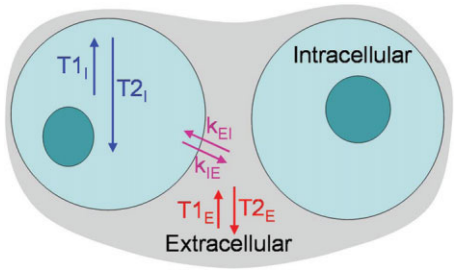

FIG. 1. Two-pool model of water relaxation in a cell pellet with transmembrane exchange. Intra- and extracellular water fractions M_{0I} and M_{0E} are represented by the sizes of the blue and gray areas, respectively. Relaxation inside the cells occurs with time constants T_{1I} and T_{2I}. Relaxation outside the cells occurs with time constants T_{1E} and T_{2E}. Water exchanges from inside the cell to outside at a rate k_{IE} and from outside cells to inside at the related rate k_{EI}.

assumed to have different longitudinal T_1 and transverse T_2 relaxation time constants: T_{1I} and T_{2I} for intracellular water; T_{1E} and T_{2E} for extracellular water. The process of water exchange between intracellular and extracellular compartments was characterized by the exchange rates k_{IE} and k_{EI}, which satisfy the equilibrium condition $k_{IE}M_{0I} = k_{EI}M_{0E}$. In this model, the longitudinal (M_z) and transverse (M_{xy}) magnetization were expressed using the coupled Bloch equations with exchange between the two pools:

$$\frac{dM_{zI}}{dt} = \frac{M_{0I} - M_{zI}}{T_{1I}} - k_{1E}M_{zI} + k_{EI}M_{zE} \qquad [2.1]$$

$$\frac{dM_{zE}}{dt} = \frac{M_{0E} - M_{zE}}{T_{1E}} - k_{EI}M_{zE} + k_{IE}M_{zI} \qquad [2.2]$$

$$\frac{dM_{xyI}}{dt} = -\frac{M_{xyI}}{T_{2I}} - k_{IE}M_{xyI} + k_{EI}M_{xyE} \qquad [2.3]$$

$$\frac{dM_{xyE}}{dt} = -\frac{M_{xyE}}{T_{2E}} - k_{EI}M_{xyE} + k_{IE}M_{xyI} \qquad [2.4]$$

Equations [2.1]–[2.4] were solved analytically for longitudinal M_z and transverse M_{xy} components using standard methods for solving differential equations. The resulting signal is a biexponential function (26):

$$S_z = S_z(S_0, M_{0I}, T_{1I}, T_{1E}, k_{IE}) \qquad [3.1]$$

$$S_{xy} = S_{xy}(S_0, M_{0I}, T_{2I}, T_{2E}, k_{IE}), \qquad [3.2]$$

where S_z and S_{xy} denote signals measured in the IR and CPMG experiments, respectively, and are proportional to the longitudinal and transverse magnetizations of the measured system. Additionally, the extracellular MRI contrast agent Gd-DTPA-BMA alters the relaxation of the extracellular water according to

$$\frac{1}{T_{1E}} = \frac{1}{T^0_{1E}} + r_1\lceil Gd\rceil_{ECS} \qquad [4.1]$$

$$\frac{1}{T_{2E}} = \frac{1}{T^0_{2E}} + r_2\lceil Gd\rceil_{ECS}, \qquad [4.2]$$

where $1/T^0_{1E}$ and $1/T^0_{2E}$ are the T_1 and T_2 relaxation rates in the absence of Gd contrast agents; r_1 and r_2 are the relaxivities of Gd-DTPA-BMA; and $[Gd]_{ECS}$ is the concentration of Gd-DTPA-BMA in the extracellular space.

Equations [3.1]–[3.2] describe measured IR and CPMG data as a function of seven parameters. In our experiments, eight IR and 48 CPMG data points were collected for four different concentrations of Gd in the extracellular space ($8 \times 48 \times 4$ points). Extracellular longitudinal and transverse relaxation times, T_{1E} and T_{2E}, for each Gd concentration were determined experimentally from the PBS slice, assuming monoexponential transverse and longitudinal behavior. Monoexponential fits using the eight IR points were used to evaluate longitudinal relaxation time, T_{1E}.

$$S^E_{IR} = S^E_0\left(1 - (1 + a)e^{-TI/T_{1E}} + ae^{-TR/T_{1E}}\right). \qquad [5]$$

Imperfections in the 180° pulse were accounted for using the fit parameter a to incorporate B_1 imperfections. The 180° imperfections were assumed to be uniform across the sample due to the large size of the transmit 3T GE body coil. The B_1 imperfection parameter, a, evaluated from the PBS image fit was used as a constant in two-pool model-fitting procedure. Similarly, the extracellular transverse relaxation time, T_{2E}, was evaluated from the PBS slice, assuming monoexponential behavior:

$$S^E_{CPMG} = S^E_0e^{-TE/T_{2E}}. \qquad [6]$$

For each Gd concentration, the values of T_{1E} and T_{2E} were fixed in Eqs. [2.1]–[2.4] and the five remaining independent two-pool model parameters, S_0, T_{1I}, T_{2I}, M_{0I} and k_{IE}, were fit. The IR and CPMG data were fit simultaneously.

For comparison of the two-pool model with the standard relaxation analysis, the IR and CPMG data from the cell slice for each Gd-DTPA-BMA concentration were fitted with a monoexponential function. These were calculated in the same manner as Eqs. [5] and [6], with the measured apparent relaxation times denoted $\langle T_1\rangle$ and $\langle T_2\rangle$. A global fit to all Gd-DTPA-BMA concentrations was also performed in the FXL, letting k_{IE} approach infinity in Eq. [2]. This results in relaxation times given by Eq. [1], where T_{1E} and T_{2E} vary according to Eq. [4].

Statistical analysis of the fitting procedure was also performed. The statistical errors in each parameter due to fitting were determined by adjusting that parameter in 1% increments and allowing the remaining parameters to vary to achieve a best fit to the data until

$$\chi^2 \geq \chi^2_0\left(1 + \frac{n_p}{N - n_p}F(n_p, N - n_p, 0.68)\right), \qquad [7]$$

where χ^2 is the reduced chi-squared value from the fit with one fixed parameter, χ^2_0 is the reduced chi-squared value with all parameters optimized, n_p is the number of param-

eters in the fit, N is the number of data points, and F is the F distribution function, calculated here for a 68% confidence interval (27).

Histology Processing

MRI data were compared to centrifuged cell sample microstructure. In particular, we evaluated average cell area and average nuclear area from histological sections. Immediately after MRI experiments, samples were fixed in 10% formalin for at least 96 h before being removed intact from the glass sample tubes and embedded in 3% agarose gel. Following paraffin embedding, three longitudinal slices through the center of the cell sample were stained: one with hematoxylin and eosin (H&E), one using terminal deoxynucleotidyl transferase-mediated 2′-deoxyuridine 5′-triphosphate nick-end labeling (TUNEL) and one with caspase-3 antibody (Cell Signaling Technology, Boston, MA, USA). Slides were examined under a light microscope (400× magnification).

ImageJ 1.36b (National Institutes of Health [NIH]) was used to make measurements of cell area and nuclear area for normal and treated apoptotic sections. For H&E-stained slides, 30 cells were measured at each Gd-DTPA-BMA concentration 5 mm from the bottom of the longitudinal slice, corresponding to the location of the MRI slice. There was no significant difference between concentrations, indicating no artifact from exposure to the contrast agent. Histology data from all concentrations were therefore averaged, resulting in 120 measurements for each histological parameter for each experimental repeat, which was enough to achieve statistical significance. For TUNEL and Caspase-3 sections, at least 60 cells from two different fields of view were counted as positively- or negatively-stained and this was used to determine the positive fraction of cells. Again no difference in apoptotic fraction was observed for different Gd-DTPA-BMA concentrations, so data from all concentrations were averaged.

Mass Spectrometry and Flow Cytometry

To evaluate whether the contrast agent remained extracellular in apoptotic cell samples, samples were centrifuged in 5 mM Gd-DTPA-BMA and left for 1 h, the maximum length of the scan time. Following this waiting period, cells were washed twice in 10 ml PBS to remove extracellular Gd-DTPA-BMA, frozen, homogenized, and centrifuged at 800*g* for 10 min to remove pieces of cell membrane and unbroken cells. The supernatant was analyzed by inductively-coupled plasma mass spectrometry for Gd content. The proportion of cells dying by mitotic arrest and mitotic catastrophe was determined by analyzing the DNA content of the cells by flow cytometry using propidium iodide and a FACSCalibur (BD Biosciences, Mississauga, ON, Canada) (28).

RESULTS

The MRI data are presented in Fig. 2. T_1 and T_2 relaxation became faster with increasing Gd concentration for both normal and apoptotic cells. However, at high Gd concentration, the relaxation appeared faster for the apoptotic samples in comparison to untreated samples (blue points in T_1 and T_2 relaxation curves). There is also relatively

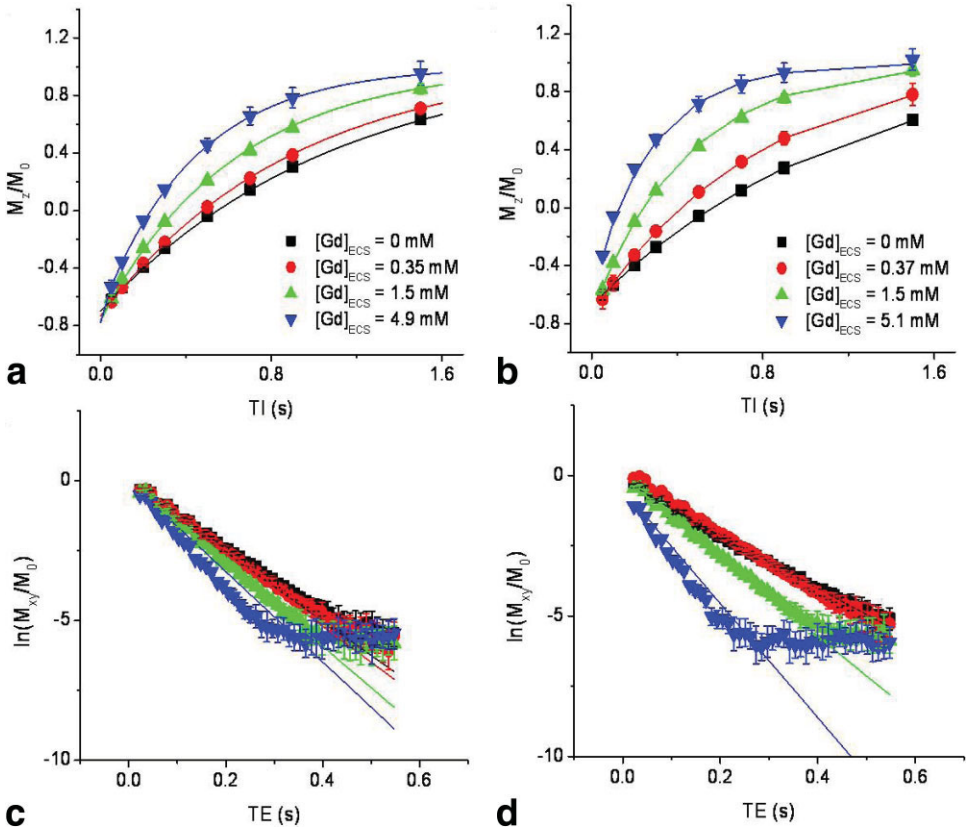

FIG. 2. Representative fits of the IR (**a**,**b**) and the CPMG (**c**,**d**) data (points) to the two-pool model (solid lines). Fits for control cells are shown on the left and for apoptotic cells on the right. Note that the fit lines deviate from CPMG data where it becomes overwhelmed by noise at late echoes and high Gd concentrations. Extracellular concentrations differ slightly between control and apoptotic samples.

good agreement between the experimental data and the fitted model curves (solid lines) with the notable exception of high Gd concentration T_2 data (Fig. 2c and d) where some systematic deviations are present. The two-pool model fit the data reasonably well—the average reduced χ^2 for the fits to control cells was 3.8 ± 1.5 and that for apoptotic cells was 6.3 ± 5.4. The high χ^2 values were due mainly to the systematic misfit of the CPMG data signal at high Gd-DTPA-BMA concentrations. The fast decay causes the noise floor to be reached during the sequence, as seen at late TEs in Figs. 2c and d, and these points cannot be fitted by the two-pool model.

In comparison, fitting in the FXL (allowing k_{IE} to approach infinity in Eq. [2], resulting in Eq. [1]) produced the dashed lines shown in Fig. 3. The average reduced χ^2 for the fits to control cells was significantly larger than that for the two-pool model (12 ± 5 for control cells and 14 ± 11 for apoptotic cells).

The two-pool model parameters for the five separate experimental trials are shown in Table 1. The average model parameters indicated a slight decrease in intracellular T_1 relaxation time, T_{1I}, from 1030 ± 50 ms in control cells to 940 ± 70 ms after apoptosis was induced. The decrease in intracellular T_2, T_{2I}, was not statistically significant. There was a decrease in intracellular water fraction, M_{0I}, from 0.86 ± 0.02 to 0.68 ± 0.07. An increase in the transmembrane water exchange from 1.4 ± 0.6 s^{-1} to 6.8 ± 3.9 s^{-1} was also observed.

The errors in the fit parameters due to the statistical procedure, determined using Eq. [7], are shown beside the values for individual experiments in Table 1. In general, they were less than the error produced by the biological variation, shown beside the mean values at the bottom of Table 1. Maximum fitting errors in T_{1I} ranged from 19 to 63 ms, compared to the biological variation of 51 ms for control and 68 ms for apoptotic cells. Errors in fitting for T_{2I} were less than 3 ms for control and 5 ms for apoptotic cells, while errors in the intracellular water fraction, M_{0I}, were <0.03 and <0.04, respectively. The statistical errors were generally symmetric around the fitted parameter value, with the notable exception of the exchange rate constant, k_{IE}. The lower bound of the fitting error was at most 0.4 s^{-1} for control cells and was much higher (3.7 s^{-1}) for apoptotic cells. The upper bound for the statistical error in the transmembrane exchange rate constant, k_{IE}, was 0.5 s^{-1} for control and 7.4 s^{-1} for apoptotic cells. The upper bound of the water exchange was more difficult to determine because a larger k_{IE} shifted the model closer to the FXL and decreased the dependence of the fit on k_{IE}. This was indicated by the larger fit error in the faster k_{IE} of apoptotic cells. No significant coupling between model parameters was observed, indicating that the model was of the minimum complexity to describe the data.

The average relaxation times, $\langle T_1 \rangle$ and $\langle T_2 \rangle$, evaluated from the monoexponential fits to the data in the absence of Gd-DTPA-BMA are also given in Table 1. At this stage of apoptosis, the average longitudinal relaxation time, T_1, was not significantly different between control and apoptotic cells. The transverse average relaxation time, T_2, increased from 90 ± 5 ms to 99 ± 7 ms, and this change was significantly different for these five experiments, although the standard deviations overlap. The average lon-

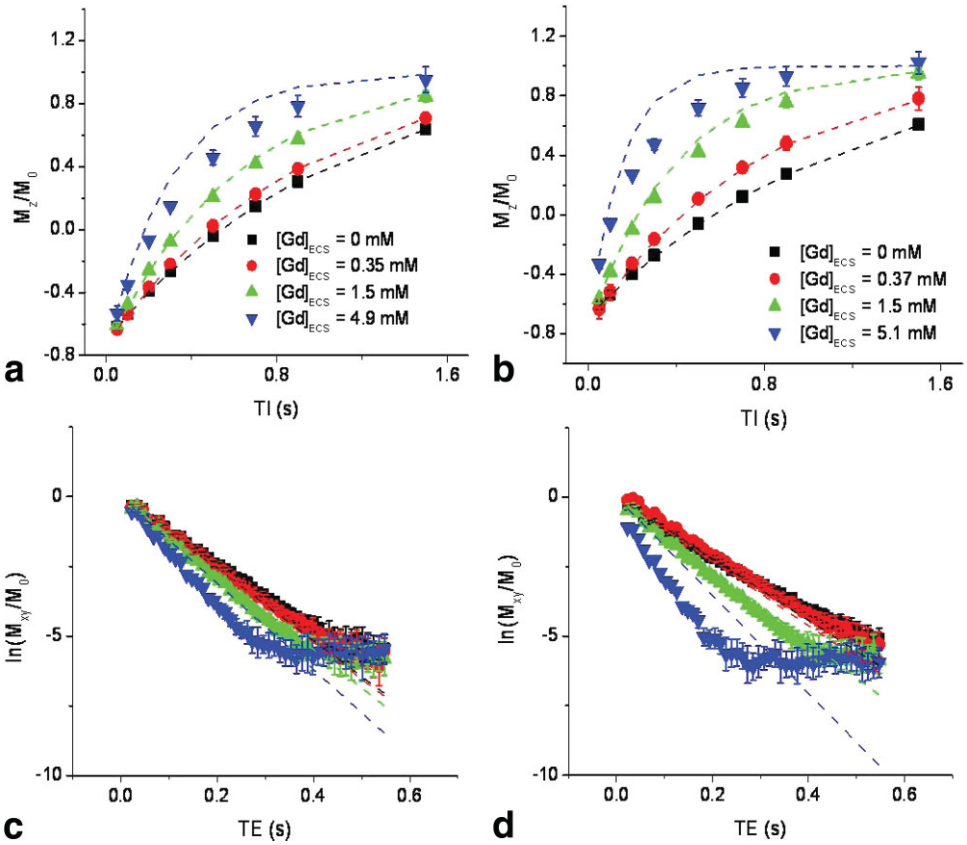

FIG. 3. Representative fits of the IR (**a**,**b**) and the CPMG (**c**,**d**) data (points) to the FXL as given by Eq. [1] (dashed lines). Fits for control cells are shown on the left and for apoptotic cells on the right. The fit can approximate T_1 relaxation at low concentrations of Gd-DTPA-BMA, but overestimates the T_1 relaxation rate and underestimates the T_2 relaxation rate in comparison to the data points at higher concentrations.

Table 1
Two-Pool Model Parameter Values for Control (C) and Apoptotic (A) Cell Pellets*

Experiment #	T_{1I} (ms)	T_{2I} (ms)	M_{0I}	k_{IE} (s^{-1})	$\langle T_1 \rangle$ (ms)	$\langle T_2 \rangle$ (ms)
1						
C	1060 ± 32	71 ± 1	0.87 ± 0.01	1.8 +0.2/−0.2	1086 ± 65	93 ± 5
A	916 ± 46	67 ± 3	0.77 ± 0.01	5.9 +1.6/−0.6	1017 ± 61	90 ± 4
2						
C	967 ± 19	60 ± 2	0.86 ± 0.01	2.2 +0.2/−0.2	1156 ± 22	82 ± 3
A	929 ± 28	53 ± 2	0.71 ± 0.01	5.5 +0.6/−0.5	1195 ± 24	95 ± 4
3						
C	1057 ± 63	68 ± 3	0.87 ± 0.02	0.7 +0.3/−0.2	1241 ± 50	91 ± 7
A	872 ± 44	47 ± 5	0.63 ± 0.03	5.3 +1.7/−1.2	1213 ± 48	103 ± 7
4						
C	992 ± 50	62 ± 3	0.85 ± 0.02	1.2 +0.4/−0.3	1141 ± 34	95 ± 12
A	924 ± 46	51 ± 4	0.61 ± 0.03	13.6 +7.4/−3.7	1224 ± 37	101 ± 4
5						
C	1087 ± 63	50 ± 4	0.83 ± 0.03	1.3 +0.5/−0.4	1022 ± 41	90 ± 5
A	1053 ± 47	40 ± 5	0.68 ± 0.04	3.9 +1.6/−1.1	1203 ± 48	108 ± 12
Mean						
C	1033 ± 51	62 ± 8	0.86 ± 0.02	1.4 +/− 0.6	1130 ± 80	90 ± 5
A	939 ± 68	52 ± 10	0.68 ± 0.07	6.8 +/− 3.9	1170 ± 86	99 ± 7
P value	<0.05	>0.1	<0.001	<0.01	>0.4	<0.05

*Intracellular longitudinal, T_{1I}, and transverse, T_{2I}, relaxation times, the intracellular water fraction, M_{0I}, and the transmembrane water exchange rate, k_{IE} are presented. Also shown are the average relaxation times, $\langle T_1 \rangle$ and $\langle T_2 \rangle$, from the monoexponential fits to the data in the absence of Gd. Errors for individual experiments are errors in the fitting procedure due to experimental noise. The standard deviation over all five experiments is shown in the last two rows beside the mean parameter values.

gitudinal and transverse relaxation times, $\langle T_1 \rangle$ and $\langle T_2 \rangle$, for all measured samples are plotted as a function of Gd-DTPA-BMA concentration in the PBS in Fig. 4. At Gd-DTPA-BMA concentrations of approximately 4 mM, the average longitudinal relaxation time, $\langle T_1 \rangle$, was 440 ms for control cells and 200 ms for apoptotic cells (Fig. 4a). Because the extracellular Gd concentration varies with the density of cells in the prepared suspension, only selected concentrations have duplicate measurements. However, the diverging nature of average relaxation rate $R_1 = 1/\langle T_1 \rangle$ for control and apoptotic cells is evident as Gd concentration increases. The difference in $R_2 = 1/\langle T_2 \rangle$ was less apparent (Fig. 4b).

The phase contrast microscope images in Fig. 5 demonstrate the changes in the AML-5 cells following cisplatin treatment. Flow cytometry confirmed that even as late as 48 h after treatment, 43% of cell death was due to apoptosis, 8% of cells were undergoing mitosis, and the remaining cells were normal, confirming no cell death by mitotic arrest or mitotic catastrophe. Histology demonstrated that all samples exhibited apoptosis 36 h after cisplatin treatment. For control cells, 4 ± 2% of cells stained positive for caspase-3 antibody compared to 58 ± 8% of cisplatin-treated cells. TUNEL staining indicated 3 ± 3% of control cells were undergoing DNA fragmentation, compared to 46 ± 29% of cisplatin-treated cells. The H&E sections indicated that 34% to 56% of cells in apoptotic samples exhibited nuclear condensation. Figure 6 shows representative images of control (Fig. 6a) and treated (Fig. 6b) sections and compares the morphological, quantitative parameters of histology with the MRI model parameters.

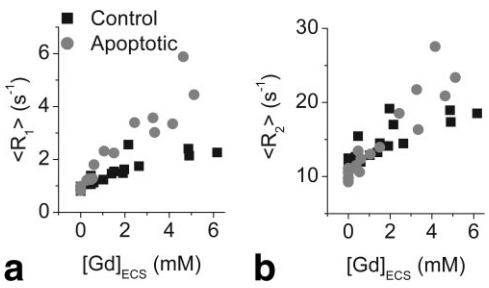

FIG. 4. Effective relaxation rates as a function of extracellular Gd-DTPA-BMA concentration. (**a**) The longitudinal relaxation rate, $R_1 = 1/T_1$, for control and apoptotic cells becomes more distinct as the concentration increases, whereas (**b**) the transverse relaxation rates, $R_2 = 1/T_2$, for control and apoptotic cells remain close.

Although the determination of intracellular volume fraction from histology was complicated by the change in cell size during fixation, agarose embedding, paraffin embedding, and artifact created during sample slicing, Fig. 6c demonstrates that the intracellular water fraction measured using MRI decreased as the cell area measured from histology decreased. This comparison assumes that the control and apoptotic cells packed similarly in the centrifuged pellets and counts of cells per unit area confirmed that there was less than 10% difference in cell density between control and apoptotic sections.

Comparison of T_{1I} with the nuclear area from histology is shown in Fig. 6d. In addition to nuclear changes, breakdown and restructuring of proteins and the cell membrane, not visible on light microscopy, are expected to influence T_{1I}. Nonetheless, an increasing trend is evident.

DISCUSSION

Figures 2 and 3 clearly demonstrate that the FXL cannot adequately fit the data and that the two-pool model is a much better approximation. Although data at low Gd-

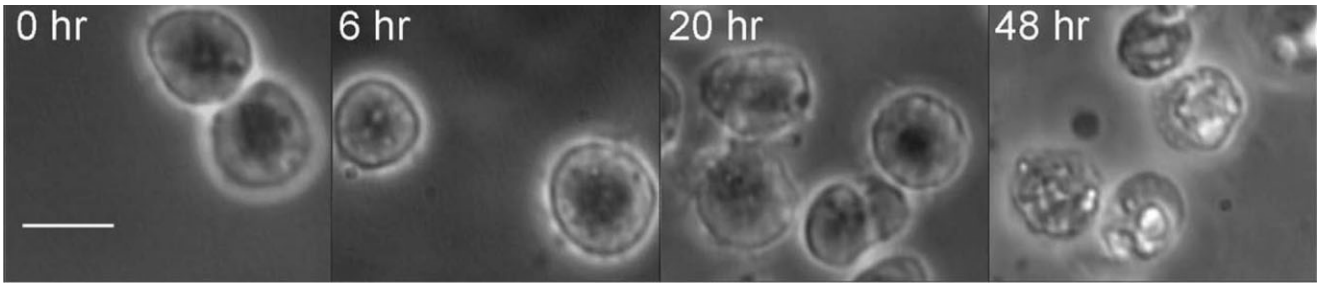

FIG. 5. Phase contrast microscope images of AML-5 cells at the indicated time points after treatment. Characteristic apoptotic changes are visible, including nuclear condensation (6–20 h); fragmentation (20 h); and membrane blebbing and cell size decrease (48 h). The scale bar represents 10 μm.

DTPA-BMA concentrations can be fit with the FXL, at high concentrations of Gd-DTPA-BMA, the T_1 relaxation rate is overestimated by this fitting method and the T_2 relaxation rate is underestimated. These systematic errors emphasize the inadequacy of the FXL and the need to include exchange when modeling relaxation in the presence of contrast agent.

Cell density in the control samples was within the range from in vivo xenograft tumors. The intracellular water fraction of the control cells, 0.86 ± 0.02, was near the median value of 0.75 determined by Yankeelov et al. (29) using dynamic contrast-enhanced MRI (DCE-MRI) of mammary carcinoma cells transplanted into mouse hind limbs where exchange was accounted for. Our reported value was, however, slightly higher than the value for cellular volume fraction of 0.67 ± 0.05 determined by scintillation counting of ^{99m}Tc-DTPA distributed in the extracellular space of excised mammary adenocarcinoma cells that had been transplanted into rats (30). This is surprising given that the intracellular water fraction is expected to be slightly less than the intracellular volume fraction due to reduced water density inside the cell in comparison to the extracellular matrix (21).

The transmembrane exchange rate is related to the permeability of the cell membrane, P, and the surface area-to-volume ratio of the cell, A_{surf}/V, by (21)

$$k_{IE} = P\frac{A_{surf}}{V}. \quad [8]$$

The average diameter of the AML-5 cells was approximately 10 μm and they were spherically shaped. Therefore, using Eq. [8], the cell membrane permeability for normal AML-5 cells can be calculated to be (0.2 ± 0.1) × 10^{-3} cm/s. This is 70% lower than the cell permeability of

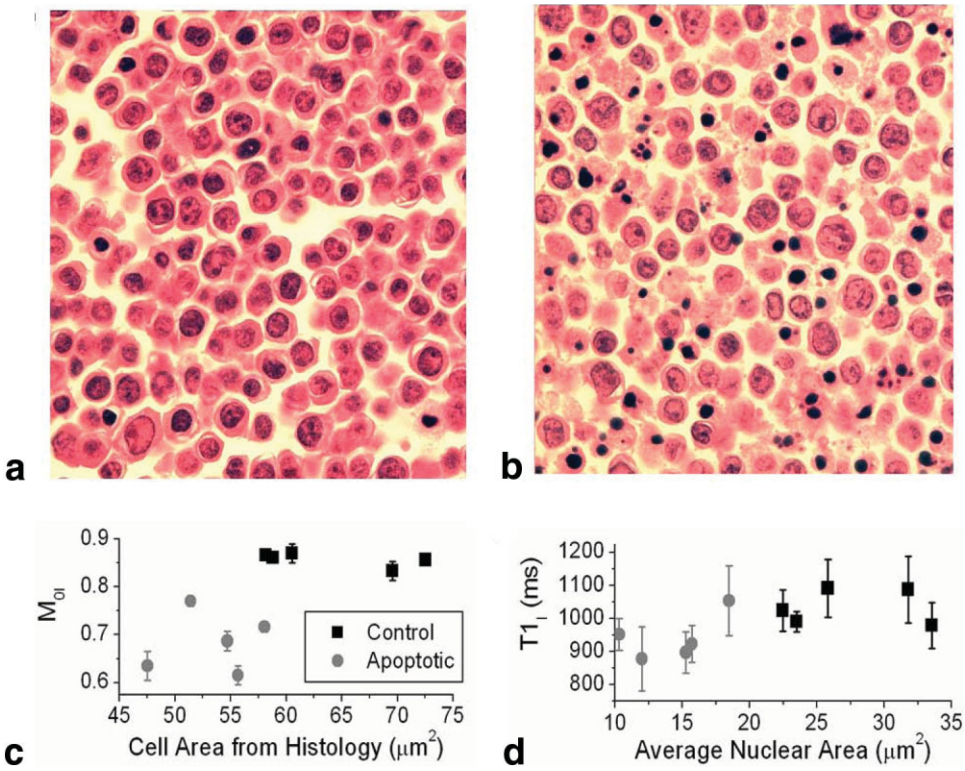

FIG. 6. Representative H&E stained sections from (**a**) a control cell sample and (**b**) a sample treated with cisplatin 36 h before fixation. Correlation between MRI parameters from the two-pool model (*y*-axis) and measurements of the cells from histology (*x*-axis) are also shown. **c:** The intracellular water fraction from MRI decreases as the cell area decreases. **d:** The intracellular T_1 relaxation time decreases as the average nuclear area decreases. The condensation of the nuclear material visible on histology occurs concurrently with the breakdown of many macromolecules in the cell.

the leakiest cell in human body, the red blood cell (31), and lower than that evaluated by Zhao et al. (32) using 20-μm-diameter human carcinoma (HeLa) cells (2.8 ± 0.3) $\times 10^{-3}$ cm/s. It was also lower than that obtained by Farinas et al. (33) for Madin-Darby canine kidney (MDCK) epithelial cells (1.1×10^{-3} cm/s) and human tracheal cells (5.2×10^{-3} cm/s).

The cisplatin-treated cells exhibited changes in the model parameters that are consistent with known apoptotic changes and with the changes visible on histology. The decrease in intracellular water fraction correlated with the decrease in cell size seen in Fig. 6c. It must be noted that the intracellular water fraction might also decrease due to a change in water density in the cytoplasm. Cell loss and shrinkage in apoptotic cells has also been observed to affect diffusion imaging as an increase in the trace of the diffusion tensor (12,13).

The slight decrease in intracellular T_1 from 1030 ± 50 ms to 940 ± 70 ms may be due to decreased water mobility in the cytoplasm or an altered magnetization transfer (MT) effect caused by macromolecular breakdown and changes in the structure of the plasma membrane. This MT hypothesis is consistent with the observed, early-stage apoptotic changes in spin-lock relaxation times, $T_{1\rho}$ and $T_{2\rho}$, which are indicative of the slower motions of large molecules (14,34–36).

The increase in transmembrane water exchange, k_{IE}, may have multiple contributions. If it is assumed that cells remain spherical and that all changes in water content are due to a decrease in cell size, the decrease in M_{0I} from 0.86 to 0.68 corresponds to a decrease in cell radius of 7.5%. The resulting increase in surface area–to–volume ratio would then account for only 8% of the increase in k_{IE}. Therefore, other mechanisms, such as alterations in cellular shape (increased surface area–to–volume ratio) or a dramatic increase in cell permeability, P, are likely responsible. Membrane blebbing was observed on histology for apoptotic cells and would result in increased surface area. Additionally, membrane integrity is lost in the late stages of apoptosis (37), leading to increased membrane permeability to water.

Since the results may indicate increased membrane permeability for water molecules due to apoptosis, it is possible that the apoptotic cell membrane is permeable for relatively small molecules such as Gd-DTPA-BMA. Leakage into the intracellular space results in increased tissue space accessible to Gd-DTPA-BMA. Obviously, in the case of Gd leakage, the two-pool model described by Eqs. [2.1]–[2.4] is no longer valid since the relaxation rates in the intracellular space are no longer constant; they decrease depending on the amount of Gd leaking into the cells. Unfortunately, MRI experiments alone cannot assess whether Gd-DTPA-BMA leaks into the cell—the nature of the relaxation decay curves is similar to the case of a purely extracellular contrast agent. However, wrong assumptions about contrast agent localization may lead to systematic errors of the two-pool model parameter estimates. This is illustrated in Table 2, which shows a hypothetical case of Gd-DTPA-BMA leakage into the intracellular space. The AML control cell parameters from Table 1 are shown in the first row and leakage data was simulated by assuming that the indicated percentages (10% and 0.7%) of Gd-DTPA-BMA leaked into the intracellular space. A 10% leakage would therefore indicate intracellular Gd-DTPA-BMA concentrations of 0, 0.035, 0.15, and 0.49 mM. The simulated data were then refit to the original two-pool model; these parameters are shown in the last two rows of Table 2. The results indicate that, for 10% leakage, the intracellular T_1 and the intracellular water fraction would be underestimated, whereas the transmembrane exchange rate constant would be overestimated. The two-pool and leakage models therefore can both accurately describe the MRI data.

Table 2
Two-Pool Fit to Data Simulating Leakage of the Indicated Percentage of Extracellular Gd-DTPA-BMA Across the Plasma Membrane to the Intracellular Compartment, Assuming no Other Cellular Changes

Parameter	T_{1I} (ms)	T_{2I} (ms)	M_{0I}	k_{IE} (s^{-1})
Control	1030	60	0.86	1.4
10% Leakage	970	53	0.77	4.5
0.7% Leakage	1030	61	0.85	1.9

In addition to mathematical simulations, possible Gd-DTPA leakage in the measured samples was evaluated by mass spectrometry of the cell lysates. This revealed that the supernatant from control cells contained 0.025 mM Gd, possibly due to imperfect washing of the cells, while the apoptotic cell lysate contained 0.034 mM Gd. This would correspond to a maximum leakage of 0.7% of the extracellular Gd-DTPA-BMA across the plasma membrane. As seen in Table 2, such a small amount of leakage does not influence the two-pool model significantly, and therefore the effects of leakage can be neglected. It must be stated, however, that at the later stages of cellular apoptosis or early necrosis, partial cell-membrane breakdown is expected, resulting in some of the Gd leaking inside the cells and causing systematic errors in the two-pool model estimates.

The analysis of model parameters in the apoptotic cells explains the relatively low sensitivity of standard monoexponential longitudinal, T_1, and transverse, T_2, relaxation measurements to early stages of apoptosis, both in the present study and in the literature (12–14). In the case of normal control cells in the absence of Gd-DTPA-BMA, the transmembrane exchange rate constant, $k_{IE} > |1/T_{1I} - 1/T_{1E}| = 0.63\ s^{-1}$, indicating that the longitudinal relaxation is in the FXL. Further increase in the exchange rate due to apoptosis does not change the exchange regime and therefore has little influence on the average relaxation, which follows Eq. [1.1]. The observed decrease in intracellular T_1 relaxation time, T_{1I}, was counterbalanced by the decreased intracellular water fraction, M_{0I}, in this faster-relaxing compartment, resulting in negligible change in the average T_1 in the absence of Gd contrast. With the addition of Gd-DTPA-BMA, the extracellular longitudinal relaxation rate, T_{1E}, became faster than T_{1I} and began to dominate the overall relaxation. Increased Gd concentration, and hence increased extracellular longitudinal relaxation rate, $1/T_{1E}$, causes a shift from the FXL to intermediate exchange regime ($k_{IE} \approx |1/T_{1I} - 1/T_{1E}|$) in control cells. The increased exchange rate and increased extracel-

lular water fraction in apoptotic cells resulted in more water accessing the fast extracellular relaxation environment per unit time. The average T_1 decreased in apoptotic cells as a result, shown by the larger difference in $\langle T_1 \rangle$ at higher concentrations of Gd-DTPA-BMA in Fig. 4a.

In contrast, the intracellular transverse relaxation rate, $1/T_{2I}$, was 16 s^{-1} for control cells, such that the decrease in the intracellular water fraction, M_{0I}, during apoptosis caused T_2 to slow. Because $|1/T_{2I} - 1/T_{2E}| = 15\ s^{-1} > k_{IE}$, the water was not in the FXL with respect to T_2 relaxation and the increased exchange rate in apoptotic cells caused $\langle T_2 \rangle$ to become slightly faster, but not enough to compensate for the M_{0I} changes. Therefore, a slight increase in $\langle T_2 \rangle$ was seen for apoptotic cells (last column of Table 1). With the addition of Gd-DTPA-BMA, the relaxation in the extracellular environment approached that in the intracellular environment, a shift toward the FXL, making the measurements of the monoexponential T_2 relaxation, $\langle T_2 \rangle$, in the presence of contrast less sensitive to the water fraction and exchange rate changes during apoptosis, demonstrated by the overlap in control and apoptotic points at high Gd concentrations in Fig. 4b.

The movement from the FXL to the intermediate exchange regime by the addition of Gd contrast agents is an important consideration in interpreting DCE-MRI data, and has been previously noted (22) and accounted for in the shutter-speed model (29,38). Failing to properly account for exchange may result in an underestimation of the DCE model parameters K_{trans}, the volume transfer constant, and v_e, the extravascular extracellular volume fraction (29).

DCE studies used to monitor antiangiogenic therapies have focused largely on the K_{trans} parameter (39,40), which reflects the permeability of the vasculature to the contrast agent. However, this study indicates that v_e, which decreased in some studies (3), could be significant in terms of cell loss or cell shrinkage due to apoptosis.

Including the transmembrane water exchange in DCE models is not only important for accurate evaluation of K_{trans} and v_e, but the transmembrane exchange rate itself is an important parameter that describes cell membrane integrity, and its changes may reflect apoptosis. The transmembrane exchange rate is therefore expected to be a key parameter in the monitoring of apoptosis following antiangiogenic, chemotherapy, or radiation therapy. It is often assumed that decreased extracellular volume fraction, v_e, indicates success of antiangiogenesis treatment and reduction in the vascular pools. However, it is possible that this parameter increases even in the case of vascular damage. This can occur when the processes of devascularization are also accompanied by apoptosis or cell death.

The present study focused on in vitro cell cultures. There are several limitations to the in vitro model that must be considered for translation to a DCE experiment. First, the amount of apoptosis observed in the cell pellet, 46% based on TUNEL staining, was quite high. Typical measurements of apoptosis in tumors have a baseline of a few percent, with a two- to six-fold increase in apoptosis in patients responding to treatment (4,5). Sensitivity of MRI to these lower levels of apoptosis may be a concern. However, it should be noted that the remnants of apoptotic cells will be cleared by macrophages in vivo, which may result in an even larger decrease in intracellular water fraction, M_{0I}, than observed in vitro, increasing the sensitivity of the model to lower percentages of apoptosis.

A second difference is the inability to measure T_{1E} or T_{2E} directly. In vivo, the formalism of the pharmacokinetic model can describe movement of contrast agent from the blood pool (where contrast agent concentration can be measured) to the extracellular space. For example, Landis et al. (38) introduced multicompartmental model formalism with exchange to analyze DCE-MRI data. Recently, Buckley et al. (41) showed that inclusion of data at different flip angles allows intracellular and extracellular water compartments and exchange to be modeled. These results showed that a multiple–flip angle method allowed K_{trans} to be determined within 10% and v_e within 7%, with no loss in accuracy compared to FXL models. The precision of the cellular residence time (reciprocal of the exchange rate) varied widely, from 36% in one patient up to 600%. However, these data were acquired with scan parameters that have not been optimized for the accurate evaluation of exchange (a limited number of exchange-sensitive small flip angle data points were acquired). Our own preliminary simulations indicated that interleaving of different flip angles would allow for more precise determination of the exchange rate, giving insight into the integrity and shape of the cell membrane.

CONCLUSIONS

Combined analysis of the longitudinal and transverse relaxation data of cell samples at a range of known extracellular Gd-DTPA-BMA concentrations allows estimation of intrinsic characteristics of water in the extracellular and intracellular compartments and the exchange rate constant between these tissue compartments. The changes in these parameters are indicative of and are consistent with known alterations in cell microstructure during apoptosis and reveal apoptotic changes and thus allow early detection of tumor response to therapy.

ACKNOWLEDGMENTS

C.B. was supported by a scholarship from the National Sciences and Engineering Research Council of Canada. Mass spectrometry assistance from Naomi Matsura and Siqi Zhu, histology work from Petia Stefanova, and suggestions from Dr. Don Plewes are greatly appreciated. Flow cytometry data were provided by Roxana Vlad.

REFERENCES

1. Blankenberg FG, Tait JF, Strauss HW. Apoptotic cell death: its implications for imaging in the next millennium. Eur J Nucl Med 2000;27:359–367.
2. Hayes C, Padhani AR, Leach MO. Assessing changes in tumour vascular function using dynamic contrast-enhanced magnetic resonance imaging. NMR Biomed 2002;15:154–163.
3. Rudin M, McSheehy PM, Allegrini PR, Rausch M, Baumann D, Becquet M, Brecht K, Brueggen J, Ferretti S, Schaeffer F, Schnell C, Wood J. PTK787/ZK222584, a tyrosine kinase inhibitor of vascular endothelial growth factor receptor, reduces uptake of the contrast agent GdDOTA by murine orthotopic B16/BL6 melanoma tumours and inhibits their growth in vivo. NMR Biomed 2005;18:308–321.

4. Ellis PA, Smith IE, McCarthy K, Detre S, Salter J, Dowsett M. Preoperative chemotherapy induces apoptosis in early breast cancer. Lancet 1997;349:849.
5. Symmans WF, Volm MD, Shapiro RL, Perkins AB, Kim AY, Demaria S, Yee HT, McMullen H, Oratz R, Klein P, Formenti SC, Muggia F. Paclitaxel-induced apoptosis and mitotic arrest assessed by serial fine-needle aspiration: implications for early prediction of breast cancer response to neoadjuvant treatment. Clin Cancer Res 2000;6:4610–4617.
6. Hakumaki JM, Brindle KM. Techniques: visualizing apoptosis using nuclear magnetic resonance. Trends Pharmacol Sci 2003;24:146–149.
7. Brindle KM. Molecular imaging using magnetic resonance: new tools for the development of tumour therapy. Br J Radiol 2003;76(Spec No 2):S111–S117.
8. Martin SJ, Green DR, Cotter TG. Dicing with death: dissecting the components of the apoptosis machinery. Trends Biochem Sci 1994;19:26–30.
9. Niendorf T, Dijkhuizen RM, Norris DG, van Lookeren Campagne M, Nicolay K. Biexponential diffusion attenuation in various states of brain tissue: implications for diffusion-weighted imaging. Magn Reson Med 1996;36:847–857.
10. Stanisz GJ, Webb S, Munro CA, Pun T, Midha R. MR properties of excised neural tissue following experimentally induced inflammation. Magn Reson Med 2004;51:473–479.
11. Lemaire L, Franconi F, Saint-Andre JP, Roullin VG, Jallet P, Le Jeune JJ. High-field quantitative transverse relaxation time, magnetization transfer and apparent water diffusion in experimental rat brain tumour. NMR Biomed 2000;13:116–123.
12. Chenevert TL, McKeever PE, Ross BD. Monitoring early response of experimental brain tumors to therapy using diffusion magnetic resonance imaging. Clin Cancer Res 1997;3:1457–1466.
13. Valonen PK, Lehtimaki KK, Vaisanen TH, Kettunen MI, Grohn OH, Yla-Herttuala S, Kauppinen RA. Water diffusion in a rat glioma during ganciclovir-thymidine kinase gene therapy-induced programmed cell death in vivo: correlation with cell density. J Magn Reson Imaging 2004;19:389–396.
14. Duvvuri U, Poptani H, Feldman M, Nadal-Desbarats L, Gee MS, Lee WM, Reddy R, Leigh JS, Glickson JD. Quantitative T_{1rho} magnetic resonance imaging of RIF-1 tumors in vivo: detection of early response to cyclophosphamide therapy. Cancer Res 2001;61:7747–7753.
15. Hakumaki JM, Liimatainen T. Molecular imaging of apoptosis in cancer. Eur J Radiol 2005;56:143–153.
16. vanTilborg GAF, Mulder WJM, Deckers N, Storm G, Reutelingsperger CPM, Strijkers GJ, Nicolay K. Annexin A5-functionalized bimodal lipid-based contrast agents for the detection of apoptosis. Bioconjug Chem 2006;17:741–749.
17. Zhao M, Beauregard DA, Loizou L, Davletov B, Brindle KM. Non-invasive detection of apoptosis using magnetic resonance imaging and a targeted contrast agent. Nat Med 2001;7:1241–1244.
18. Czarnota GJ, Kolios MC, Abraham J, Portnoy M, Ottensmeyer FP, Hunt JW, Sherar MD. Ultrasound imaging of apoptosis: high-resolution non-invasive monitoring of programmed cell death in vitro, in situ and in vivo. Br J Cancer 1999;81:520–527.
19. Blankenberg FG, Storrs RW, Naumovski L, Goralski T, Spielman D. Detection of apoptotic cell death by proton nuclear magnetic resonance spectroscopy. Blood 1996;87:1951–1956.
20. Blankenberg FG, Katsikis PD, Storrs RW, Beaulieu C, Spielman D, Chen JY, Naumovski L, Tait JF. Quantitative analysis of apoptotic cell death using proton nuclear magnetic resonance spectroscopy. Blood 1997;89:3778–3786.
21. Stanisz GJ, Li JG, Wright GA, Henkelman RM. Water dynamics in human blood via combined measurements of T_2 relaxation and diffusion in the presence of gadolinium. Magn Reson Med 1998;39:223–233.
22. Donahue KM, Weisskoff RM, Chesler DA, Kwong KK, Bogdanov AA Jr, Mandeville JB, Rosen BR. Improving MR quantification of regional blood volume with intravascular T_1 contrast agents: accuracy, precision, and water exchange. Magn Reson Med 1996;36:858–867.
23. Gupta RK, Ferretti JA, Becker ED, Weiss GH. A modified fast inversion-recovery technique for spin-lattice relaxation measurements. J Magn Reson 1980;38:447–452.
24. Poon CS, Henkelman RM. Practical T_2 quantitation for clinical applications. J Magn Reson Imaging 1992;2:541–553.
25. McConnell HM. Reaction rates by nuclear magnetic resonance. J Chem Phys 1958;28:430–431.
26. Landis CS, Li X, Telang FW, Molina PE, Palyka I, Vetek G, Springer CS Jr. Equilibrium transcytolemmal water-exchange kinetics in skeletal muscle in vivo. Magn Reson Med 1999;42:467–478.
27. Bevington PR, Robinson DK. Data reduction and error analysis for the physical sciences. Boston: McGraw-Hill; 2003. 320 p.
28. Vlad RM, Alajez NM, Giles A, Kolios MC, Czarnota GJ. Quantitative ultrasound characterization of cancer radiotherapy effects in vitro. Int J Radiat Oncol Biol Phys 2008;72:1236–1243.
29. Yankeelov TE, Luci JJ, DeBusk LM, Lin PC, Gore JC. Incorporating the effects of transcytolemmal water exchange in a reference region model for DCE-MRI analysis: theory, simulations, and experimental results. Magn Reson Med 2008;59:326–335.
30. Donahue KM, Weisskoff RM, Parmelee DJ, Callahan RJ, Wilkinson RA, Mandeville JB, Rosen BR. Dynamic Gd-DTPA enhanced MRI measurement of tissue cell volume fraction. Magn Reson Med 1995;34:423–432.
31. Benga G. Water transport in red blood cell membranes. Prog Biophys Mol Bio 1988;51:193–245.
32. Zhao L, Kroenke CD, Song J, Piwnica-Worms D, Ackerman JJ, Neil JJ. Intracellular water-specific MR of microbead-adherent cells: the HeLa cell intracellular water exchange lifetime. NMR Biomed 2008;21:159–164.
33. Farinas J, Kneen M, Moore M, Verkman AS. Plasma membrane water permeability of cultured cells and epithelia measured by light microscopy with spatial filtering. J Gen Physiol 1997;110:283–296.
34. Grohn OH, Valonen PK, Lehtimaki KK, Vaisanen TH, Kettunen MI, Yla-Herttuala S, Kauppinen RA, Garwood M. Novel magnetic resonance imaging contrasts for monitoring response to gene therapy in rat glioma. Cancer Res 2003;63:7571–7574.
35. Sierra A, Michaeli S, Niskanen JP, Valonen PK, Grohn HI, Yla-Herttuala S, Garwood M, Grohn OH. Water spin dynamics during apoptotic cell death in glioma gene therapy probed by T(1rho) and T(2rho). Magn Reson Med 2008;59:1311–1319.
36. Hakumaki JM, Grohn OH, Tyynela K, Valonen P, Yla-Herttuala S, Kauppinen RA. Early gene therapy-induced apoptotic response in BT4C gliomas by magnetic resonance relaxation contrast T_1 in the rotating frame. Cancer Gene Ther 2002;9:338–345.
37. Baisch H, Bollmann H, Bornkessel S. Degradation of apoptotic cells and fragments in HL-60 suspension cultures after induction of apoptosis by camptothecin and ethanol. Cell Proliferat 1999;32:303–319.
38. Landis CS, Li X, Telang FW, Coderre JA, Micca PL, Rooney WD, Latour LL, Vetek G, Palyka I, Springer CS Jr. Determination of the MRI contrast agent concentration time course in vivo following bolus injection: effect of equilibrium transcytolemmal water exchange. Magn Reson Med 2000;44:563–574.
39. Yu HJ, Chen J, Mehta RS, Nalcioglu O, Su M. MRI measurements of tumor size and pharmacokinetic parameters as early predictors of response in breast cancer patients undergoing neoadjuvant anthracycline chemotherapy. J Magn Reson Imaging 2007;26:615–623.
40. Li KL, Wilmes LJ, Henry RG, Pallavicini MG, Park JW, Hu-Lowe DD, McShane TM, Shalinsky DR, Fu YJ, Brasch RC, Hylton NM. Heterogeneity in the angiogenic response of a BT474 human breast cancer to a novel vascular endothelial growth factor-receptor tyrosine kinase inhibitor: assessment by voxel analysis of dynamic contrast-enhanced MRI. J Magn Reson Imaging 2005;22:511–519.
41. Buckley DL, Kershaw LE, Stanisz GJ. Cellular-interstitial water exchange and its effect on the determination of contrast agent concentration in vivo: dynamic contrast-enhanced MRI of human internal obturator muscle. Magn Reson Med 2008;60:1011–1019.